REPORT DOCUMENTATION PAGE

Form Approved OMB No. 0704-0188

Public reporting burden for this collection of information is estimated to average 1 hour per response, including the time for reviewing instructions, searching existing data sources, gathering and maintaining the data needed, and completing and reviewing the collection of information. Send comments regarding this burden estimate or any other aspect of this collection of information, including suggestions for reducing the burden, to Department of Defense, Washington Headquarters Services, Directorate for Information Operations and Reports (0704-0188), 1215 Jefferson Davis Highway, Suite 1204, Arlington, VA 22202-4302. Respondents should be aware that notwithstanding any other provision of law, no person shall be subject to any penalty for failing to comply with a collection of information if it does not display a currently valid OMB control number.
PLEASE DO NOT RETURN YOUR FORM TO THE ABOVE ADDRESS.

1. REPORT DATE *(DD-MM-YYYY)* 04-10-2010	2. REPORT TYPE Final Report	3. DATES COVERED *(From – To)* 1 July 2007 - 01-Jul-10

4. TITLE AND SUBTITLE Bypass Transition in Turbomachinery Flows: Turbulent Spots and The Calming Effect	5a. CONTRACT NUMBER FA8655-07-1-3009
	5b. GRANT NUMBER
	5c. PROGRAM ELEMENT NUMBER
6. AUTHOR(S) Professor Tamer A Zaki	5d. PROJECT NUMBER
	5d. TASK NUMBER
	5e. WORK UNIT NUMBER

7. PERFORMING ORGANIZATION NAME(S) AND ADDRESS(ES) Imperial College London Exhibition Road London SW7 2AZ United Kingdom	8. PERFORMING ORGANIZATION REPORT NUMBER N/A

9. SPONSORING/MONITORING AGENCY NAME(S) AND ADDRESS(ES) EOARD Unit 4515 BOX 14 APO AE 09421	10. SPONSOR/MONITOR'S ACRONYM(S)
	11. SPONSOR/MONITOR'S REPORT NUMBER(S) Grant 07-3009

12. DISTRIBUTION/AVAILABILITY STATEMENT

Approved for public release; distribution is unlimited.

13. SUPPLEMENTARY NOTES

14. ABSTRACT

Direct numerical simulations (DNS) were carried out of bypass transition in favorable, zero, and adverse pressure gradient boundary layers in the presence of free-stream turbulence. A time sequence from the ZPG simulations was stored in order to obtain a number of spots for the study of the calming effect. Since the previous report on the research, additional spots have been obtained, in order to increase the number of available events to forty two (42) spots. Various flow visualization techniques were used to analyze the evolution of the spots. It was observed that the location of spot inception is difficult to identify. In the previous report, the investigator analyzed the instability of the streaky boundary layer. The investigator herein report the use of the Lyapunov Exponent in order to determine the Lagrangian Coherent Structures (LCS), which form the spot. Additionally, work was done to determine the average spot inception location, spreading rate, and speed of propagation.

15. SUBJECT TERMS

EOARD, Transition, Turbomachinery

16. SECURITY CLASSIFICATION OF:			17. LIMITATION OF ABSTRACT UL	18, NUMBER OF PAGES	19a. NAME OF RESPONSIBLE PERSON Brad Thompson
a. REPORT UNCLAS	b. ABSTRACT UNCLAS	c. THIS PAGE UNCLAS		32	19b. TELEPHONE NUMBER *(Include area code)* +44 (0)1895 616163

Standard Form 298 (Rev. 8/98)
Prescribed by ANSI Std. Z39-18

Bypass transition to turbulence and the anatomy of turbulent spots

Contract FA8655-07-1-3009†
Final report
July 2010

Table of contents

List of figures

List of tables

4

Summary

Direct numerical simulations (DNS) were carried out of bypass transition in favorable, zero, and adverse pressure gradient boundary layers in the presence of free-stream turbulence. A time sequence from the ZPG simulations was stored in order to obtain a number of spots for the study of the calming effect. In the last six months, additional spots have been obtained, in order to increase the number of available events to forty two (42) spots. Various flow visualization techniques were used to analyse the evolution of the spots. It was observed that the location of spot inception is difficult to identify. In the previous report, we analyzed the instability of the streaky boundary layer. We herein report the use of the Lyapunov Exponent in order to determine the Lagrangian Coherent Structures (LCS), which form the spot. We also report on our effort to determine the average spot inception location, spreading rate, and speed of propagation.

1. Introduction

1.1. *Bypass transition*

Boundary layer breakdown to turbulence is generally classified into two distinct types: The first, natural or orderly transition, is prevalent in low disturbance environments and proceeds via the amplification and breakdown of Tollmien-Schlichting (TS) waves. The second type is the 'bypass' scenario. It is preceded by the amplification of boundary layer perturbation streaks, or Klebanoff modes. The streaks can amplify to levels of 10 − 15% of the free-stream velocity, U_∞, and breakdown at low Reynolds numbers, hence 'bypassing' the natural route. The bypass scenario prevails in conditions of free stream turbulence above 1% of the free stream velocity, and is therefore important for many engineering flows. An integral part of the bypass process is the secondary instability of boundary layer streaks (Swearingen & Blackwelder 1987; Andersson *et al.* 2001), which leads on to the formation of turbulent spots (see figure 1.1). These spots are sporadic patches of turbulence which grow and merge to sustain the upstream edge of the fully turbulent boundary layer.

The significance of turbulent spots is widely acknowledged, and they display a variety of interesting phenomena. For instance, the area trailing the turbulent spots, known as the calmed region, has been shown to have a stabilizing effect on the flow with significant implications for separation delay (see for example Johnson 2001).

1.2. *Influence of turbulent spots on boundary layer separation*

In adverse pressure gradient, boundary layers are prone to separation and, as a result, loss of lift and higher viscous losses. One example is the flow in turbo-machinery, particularly in the compressor passages, due to the adverse pressure condition.

Figure 2 is an illustration of the instantaneous laminar flow around a compressor blade, from direct numerical simulations (Zaki *et al.* 2009, 2010). Contours of instantaneous vorticity capture the separated boundary layers on both sides of the blade. On the pressure surface, the separation rolls remain adjacent to the surface. The dynamics on the suction surface are more complex. The interaction of the separated Kelvin–Helmholtz (K-H) rolls and the newly formed boundary layer is shown, at four phases of the shedding cycle, in figure 3(a − d). It is seen that the Kelvin–Helmholtz vortices convect slightly away from the wall. However, they maintain a separation region in their shadow, within the newly formed boundary layer. This interaction is similar to that reported in Jones *et al.* (2008).

Separation, however, can be delayed or bypassed if the laminar separation point is

6
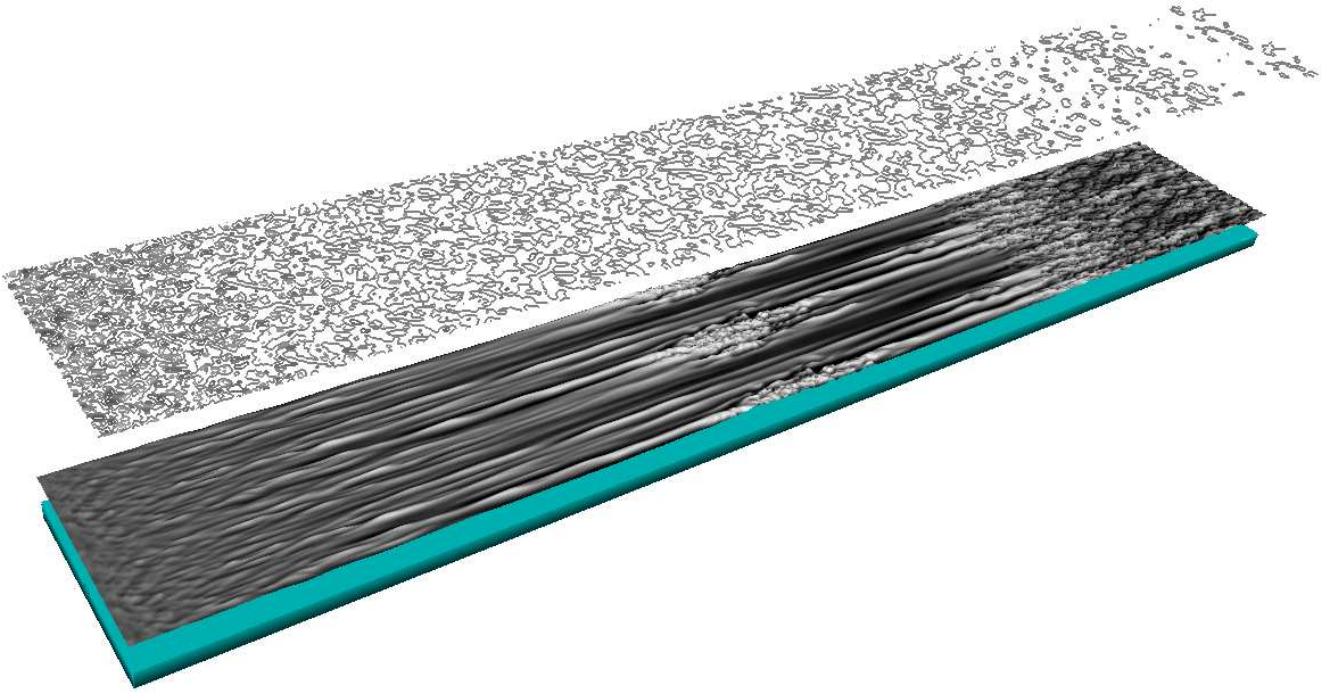
FIGURE 1. A boundary layer undergoing bypass transition due to free-stream turbulence. Contours of the instantaneous streamwise velocity perturbation are contrasted at two planes: one inside the boundary layer and one in the free stream. The former is characterized by elongated Klebanoff distortions and sporadic bursts of turbulent patches. The domain is duplicated in the periodic spanwise direction.

preceded by boundary layer transition to turbulence. Indeed, the simulations by Zaki *et al.* (2009), and in a later paper by Zaki *et al.* (2010), demonstrate that both migrating wake sand free-stream turbulence can trigger bypass transition upstream of separation. If the transition process is complete upstream of separation, the boundary layer remains attached. A time sequence which captures this behavior is shown in figure 4. When the turbulent spots form upstream of separation, they spread as they propagate downstream and cause local re-attachment. This process is intermittent: local re-attachement events are separated by relaxation of the boundary layer towards the laminar separated state.

In order to demonstrate the calming effect, the tangential velocity is plotted at a point within the separation region versus time in figure 5. The figure captures the influence of the convected turbulent spot: Initially, a more pronounced separation is observed at the spot leading edge, followed by local re-attachment of the boundary layer. The re-attachment is abrupt, and persists beyond the period of spot passing. The boundary layer indeed separates again after the spot has traveled downstream, but the relaxation to that state is relatively slow, and is associated with the calming effect of the spot.

1.3. *The anatomy of turbulent spots*

Previous experimental literature have lead to three main conclusions concerning the universality of the shape and kinematics of the turbulent patches. Firstly, the shape of turbulent spots resembles an arrowhead pointing in the positive streamwise direction.
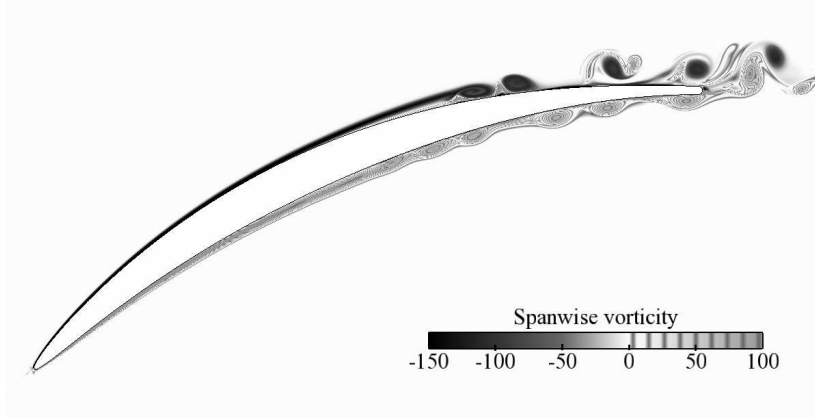
FIGURE 2. Snapshot of the vorticity field in the disturbance-free simulation T0.
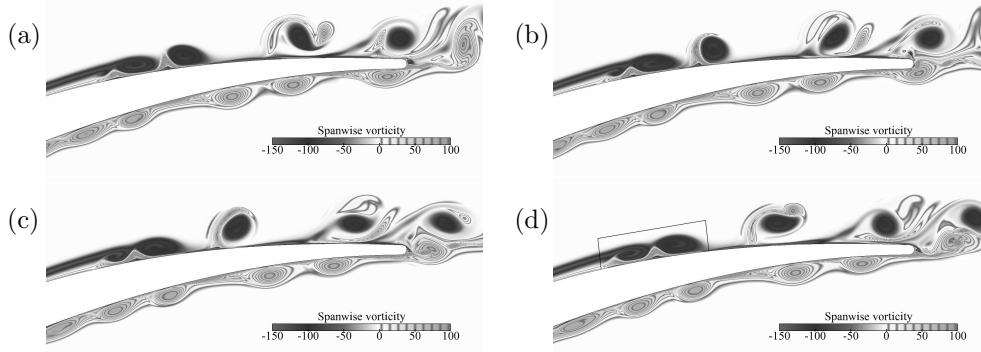
FIGURE 3. Four phases of the shedding cycle from the disturbance-free simulation T0. Total period is $T = 0.24$, which corresponds to non-dimensional frequency, $F \equiv 10^6 \omega \nu / U_o^2 = 189$

Secondly, the tip of the spot leading edge is elevated and overhangs laminar unperturbed fluid. Finally, the shape of the spot appears to be self-similar as it evolves following approximately a conical similarity, which was proposed by Cantwell *et al.* (1978) and later used by several studies including Vasudevan *et al.* (2001) and the more recent Sabatino & Smith (2008). This conical similarity is based on an observation that the spot spreads in a linear fashion in the streamwise direction, with an approximately constant spanwise spread angle of about 20 degrees. The trailing edge (TE) and the leading edge (LE) attain constant streamwise propagation speeds. The LE moves at speed approximately equal to 90% of the free-stream velocity, while the trailing edge propagation speed is on the order of 50% of the free-stream speed. The difference in propagation speeds causes an elongation of the spot as it travels downstream.

The mechanism for the spreading of turbulent spot has also been the subject of previous investigations. The laminar-turbulent interface evolves as the spot convects downstream and increases in extent. Two possible entrainment processes have been put forward: The first process is 'nibbling', which involves the propagation of the laminar-turbulent interface by means of small scale, viscous diffusion of vorticity. This mechanism is dominant in the wall-normal spreading of the spot (Cantwell *et al.* 1978). However, in the horizontal plane, the spread of the spot is via the second, more complex mechanism. This involves a

8
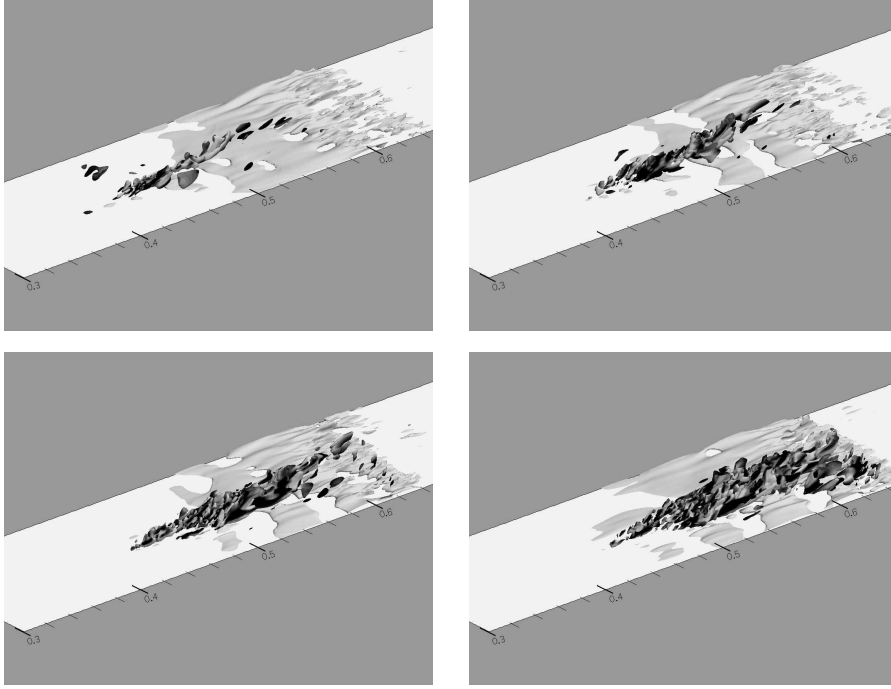
FIGURE 4. A time sequence showing the inception of a turbulent spot on the suction surface of the compressor blade. An iso-surface showing separation is also shown. The spot convects downstream and spreads downwards towards the wall. It causes local re-attachment.

destabilization of the laminar region outside the spot due to the turbulent eddies within the turbulent patch (Riley & Gad-el Hak 1985).

The structure of turbulent spots has been described as a series of large-scale spanwise vortices (see Wygnanski *et al.* 1976; Cantwell *et al.* 1978). However, recent flow visualizations have yielded a more complex structure, including hairpin vortices and streamwise oriented streaky structures (Sabatino & Smith 2008). These hairpins contribute to the lateral growth of the spot, also influencing the entrainment process at the overhung region of the leading edge (Krishnan & Sandham 2007).

The random nature of spot formation has caused difficulty in experimentally studying their evolution. In order to overcome this problem and control the location of spot inception, researchers have employed various methods of triggering spots. For instance, Cantwell *et al.* (1978) conducted experiments in a water channel, and initiated spots by tapping the wall of the channel. Gad-el Hak *et al.* (1981) carried out experiments in which turbulent spots were triggered by means of a solenoid valve ejecting fluid through the flat plate into the boundary layer. The turbulent spots in the majority of these studies can be considered as artificially triggered. Naturally-triggered spots, on the other hand, are sporadic and difficult to capture. Jacobs & Durbin (2001) conducted DNS of a zero pressure gradient boundary layer, subjected to free stream turbulence (FST) only. The spots that were observed were caused by the interaction of lifted low-speed streaks and free-stream eddies at the edge of the boundary layer. We herein discuss our recent
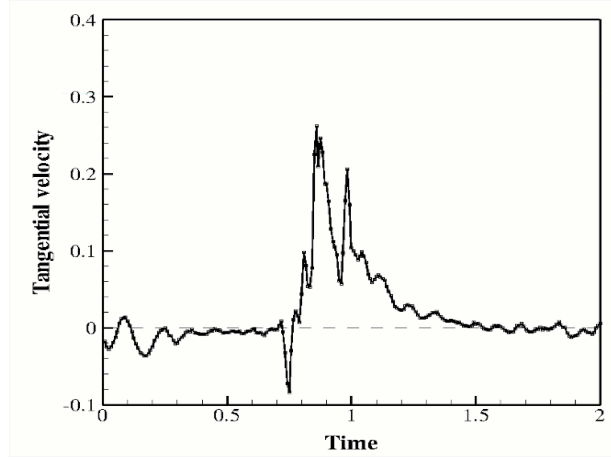
FIGURE 5. The tangential velocity near the suction surface wall is plotted versus time. The time series is taken at a point downstream of the laminar separation location. The figure shows the influence of the passing turbulent spot, and the calming effect.
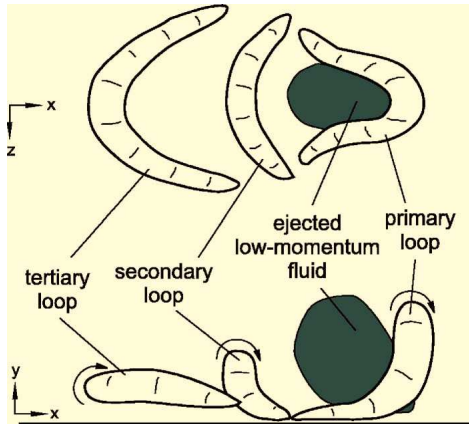
FIGURE 6. Schematic structure of the vortex loops produced in early stages of spot inception from McAuliffe & Yaras (2008).
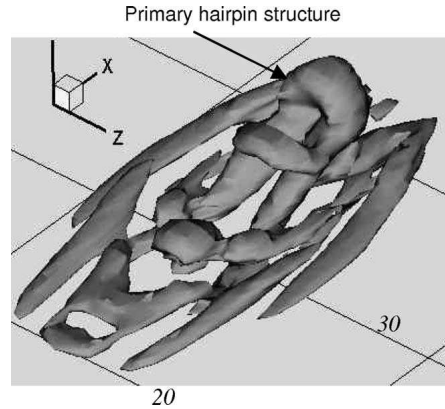
FIGURE 7. Primary Hairpin vortices along with subsequent vortex loops in the early stages of a turbulent spot using the λ_2 criterion, fromKrishnan & Sandham (2006).

progress on applying visualization technique based on the Lyapunov exponent in order to track the evolution of the spots.

2. Methods, Assumptions, and Procedures

2.1. *Direct numerical simulations of bypass transition*

Despite the moderate Reynolds number in transitional flows, the computational cost of DNS is still large. For instance, the inflow plane to the DNS domain must be place upstream of the leading edge of the plate in order to allow sufficient time for the synthesized inlet turbulence to adjust and become a solution to the Navier-Stokes equations. In ad-
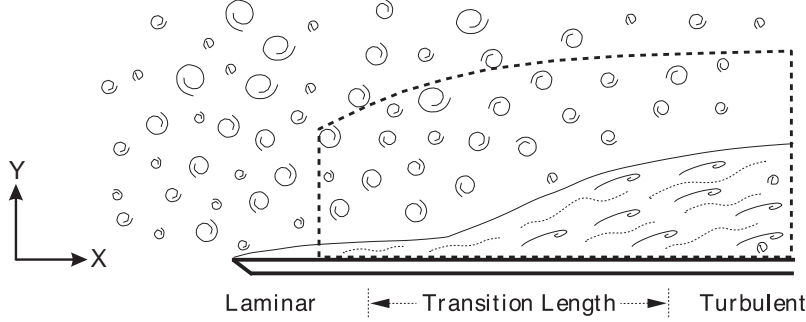
FIGURE 8. Schematic of the DNS domain. The domain boundary is indicated by the dashed line. The curvature of the top boundary ensure a constant streamwise pressure gradient parameter.

dition, the leading-edge region must be fully resolved, which significantly increases the grid requirements.

An alternative approach which reduces these constraints was proposed by Jacobs & Durbin (2001), and is also used in the current investigation. A schematic of their DNS domain is shown in figure 8. The computational domain is denoted by the dashed line, and commences at $R_\theta = 80$ which is downstream of the edge of the plate and upstream of the transition region. This choice of inflow location reduces the grid requirements for the simulations.

The inlet perturbation is synthesized as a superposition of continuous Orr-Sommerfeld and Squire modes. The continuous modes are vortical eigenfunctions of the linearized perturbation equations. Th shape of these modes resembles sines and cosines in the free-stream. Therefore, they can easily be used to synthesize a particular turbulence spectrum, with randomized phase. Inside the boundary layer, the modes decay as they approach the wall. Their decay is consistent with the solution of the linear perturbation equation, and hence do not need a significant downstream length within the computational domain to adjust to the solution of the Navier-Stokes equations.

The domain size, in terms of inflow δ_{99}, is $525 \times 30 \times 32$ in the streamwise, wall-normal, and spanwise directions. The number of grid points in each of the coordinates was $1793 \times 193 \times 193$, respectively. The top boundary of the computational domain is curved. The curvature is designed to ensure a constant pressure gradient parameter, $\lambda_\theta \equiv (\theta^2/\nu)(dU_\infty/dx)$, or equivalently a constant Falkner-Skan parameter, β, where $U_\infty(x) = Kx^{\beta/(2-\beta)}$. Four such DNS were carried out, at $\lambda_\theta = \{2,\ 0,\ -2,\ -3\} \times 10^{-2}$. All four simulations impose a zero pressure gradient profile at the inlet, which evolves downstream into the correct pressure gradient parameter.

An instance of the boundary layer disturbance field is shown in figure 9. The two panes show the streamwise u- and wall-normal v-perturbations inside the boundary layer. The u-perturbations show the large-amplitude streaks, or Klebanoff distortions. Both panes show a turbulent spot, and the downstream fully-turbulent boundary layer.

2.2. The free-stream turbulence

The literature on bypass transition has clearly demonstrated the importance of clearly documenting the free-stream turbulence conditions when comparing the influence of flow parameters, for instance pressure gradient, on transition location. In our DNS, the free-stream turbulence intensity exhibits the same time history among all simulations. This
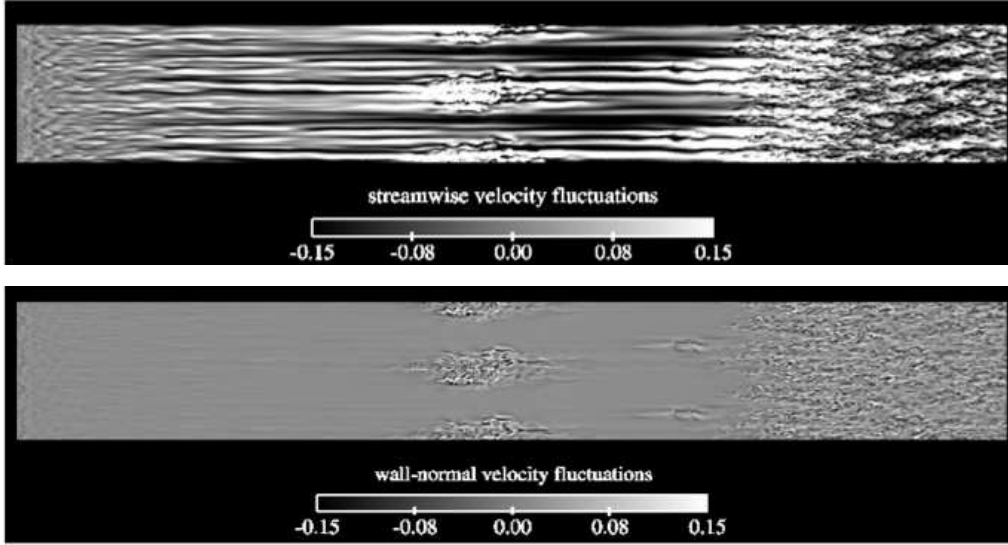
FIGURE 9. A boundary layer undergoing bypass transition due to free-stream turbulence. Contours of the instantaneous streamwise (top) and wall-normal (bottom) velocity perturbations. The $u-$perturbations clearly shows the elongated, high-amplitude Klebanoff distortions. Both panes show the turbulent spot, and downstream fullty-turbulent boundary layer. The domain is duplicated in the periodic spanwise direction.

ensures that spot inception and spreading rates can be compared in a meaningful manner. The turbulence intensity from all four simulations are shown in figure 10. It is clear that, independent of the pressure gradient, the turbulence in the free-stream decays similarly in downstream. Any changes in the transition process can therefore be attributed to the mean pressure gradient, rather than the intensity of the free-stream forcing.

The average location of transition onset, and the transition length, are generally obtained from the time-averaged skin-friction, C_f, which is shown in figure 11. All four curves start at the zero pressure gradient level, since the inflow is a Blasius profile plus free-stream turbulence. Downstream, the profiles adjust to the respective skin friction levels, for the laminar Falkner-Skan solution. Further downstream, transition to turbulence takes place. The figure shows that adverse pressure gradient, as expected, causes early transition to turbulence, and a shorter transition extent in comparison to the zero and finally adverse pressure gradient.

The length of the computational domain was deemed insufficient for the zero and favorable pressure gradient simulations. For this, and other reasons discussed below, a new simulations was carried out during the first six months of the project. The new simulation extends the computational domain to $x/\delta = 600$ instead of $x/\delta = 525$, and therefore ensures that the transition process is complete far upstream of the exit plane.

2.3. *Extended simulation domain*

The time-averaged skin friction curve in figure 11 suggest the streamwise extent of the domain is insufficiently long for the zero and favorable pressure gradient simulations. In order to ensure domain size independence, the streamwise extent of the domain must be extended and the simulations repeated for those conditions. It was therefore decided
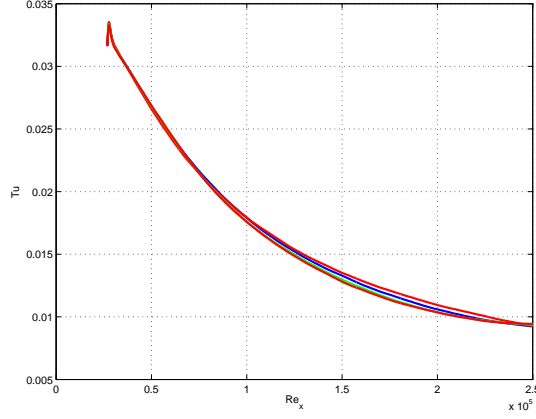
FIGURE 10. Time-averaged turbulent intensity, T_u, for various values of λ, the pressure gradient parameter.
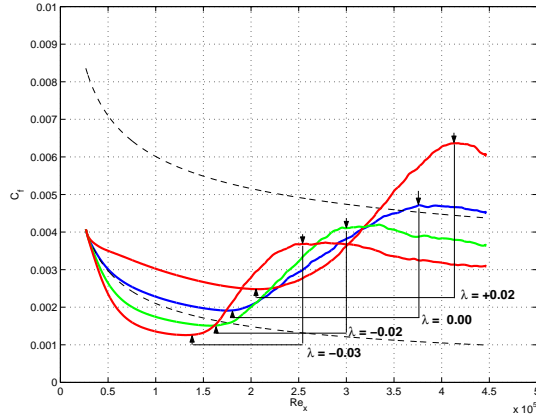
FIGURE 11. Time-averaged skin friction, C_f, for various values of λ, the pressure gradient parameter.

that a longer domain size is need in order to ensure that the spreading of the turbulent spots is unaffected by the outflow boundary conditions.

In addition, after discussion with Dr. John Clark at the AFOSR–JPR in Long Beach, California (2007), it was agreed that the number of turbulent spots from the previous simulation might be limiting in the convergence of the proposed statistical study. Therefore, a longer time period of the DNS simulation must be stored in order to accumulate sufficient turbulent spots for converged statistics.

New simulations were carried out for the zero and favorable pressure gradient simulations. The computational domain for these simulations extends to $x/\delta_{99} = 600$. The time-averaged skin friction curves for the new domain are shown in figure 12. The streamwise extent is now sufficiently long to ensure independence of the boundary layer evolution from exit boundary conditions, for the zero pressure gradient simulation. The FPG
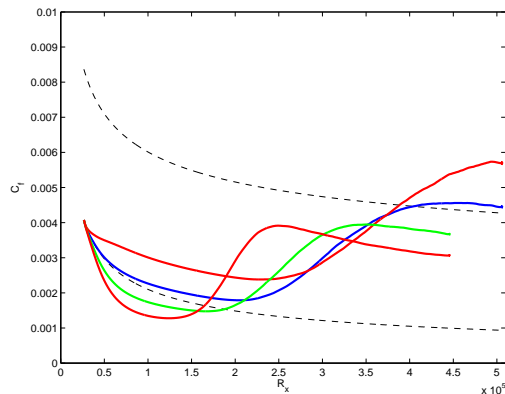
FIGURE 12. Time-averaged skin friction, C_f, in the zero pressure gradient. This new simulation has a longer streamwise domain.

simulation, on the other hand, is still transitional near the exit plane. As a result, the late stages of transition are not reliable since they can be affected by the exit boundary conditions.

Snapshots of the full velocity field were stored throughout the simulation, every two convective time units. The total number of snapshots is 4000, and they correspond to the flow traveling the transition length more than 36 times. It is therefore expected that sufficient spots will be available for post-processing. In order to reduce the storage requirements, the DNS fields are only stored every two time units, based on the convective time-scale. In addition only every third point of the DNS field is included in the output field. The requires storage from the zero pressure gradient simulation is still 0.9 Tera-Bytes.

2.4. *Visualization of the turbulent spots*

The challenge in identifying the turbulent spots is two-fold. Firstly, the spots are sporadic in nature; their inception location and time are unknown *a priori*. In DNS, the simulation can be restarted when elevated instantaneous skin-friction levels are detected at the wall, and the spot evolution is recorded. The second difficulty is due to the presence of high-amplitude disturbances throughout the boundary layer. For instance, the amplification of boundary layer streaks can interfere with the ability to detect the spot. This is demonstrated in figure 13 where the time evolution of a turbulent spot is shown using contours of $u-$perturbation velocity. Instead, use of vertical perturbation velocity contours, shown in figure 14, is likely to result in better spot detection.

Various spot detection algorithms have been tested during the first phase of the project. Each method was assessed in terms of its ability to accurately describe the shape of the spot, its spread angle, and its propagation speed. A number of the employed visualization techniques were based on iso-surfaces of physical flow quantities. These methods shared one drawback, which relates to the dependence of spot size on the threshold of the selected iso-surface. An alternative approach based on the Lyapunov exponent, and which does not share that drawback, is also considered in this section.
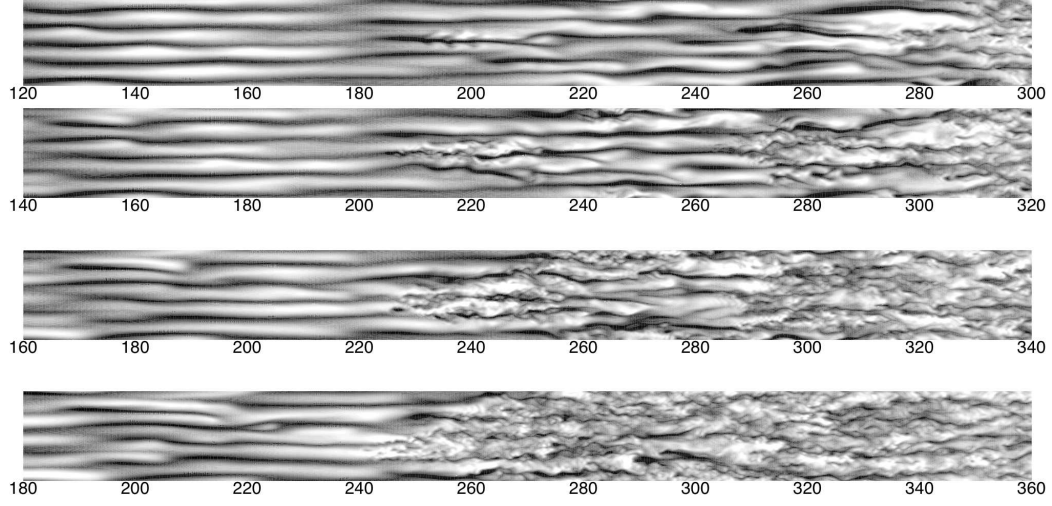
FIGURE 13. Instantaneous contours of streamwise velocity fluctuation $(-0.2 \leq u \leq 0.2)$ in ZPG bypass transition. The plane is located at $y/\delta_0 = 0.74$, and the frames translate in the flow direction at half the free-stream velocity.

FIGURE 14. Instantaneous contours of wall-normal velocity fluctuation $(-0.05 \leq v \leq 0.05)$ in ZPG. The plane is located at $y/\delta_0 = 0.74$, and the frames correspond to the same time instants as in figure 13.

15

2.5. *Computation of the Lyapunov exponent*

Time-periodic dynamical systems can be characterized by their fixed points and seperatrices which distinguish regions with different dynamical behavior. For example, the seperatrix on the 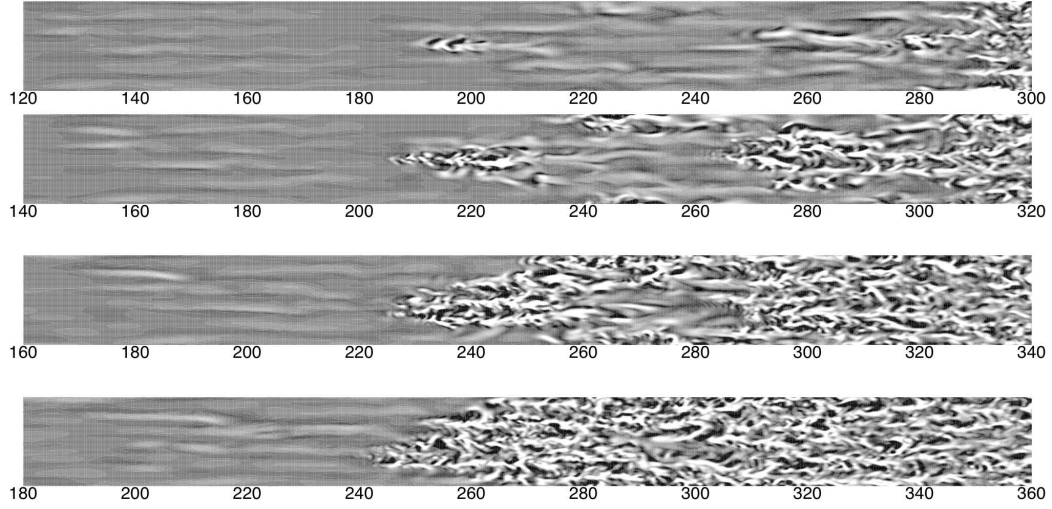phase plane of the simple pendulum system seperates the stable modes (pendulum's angular position always less than π rads) and the unstable modes (pendulum rotating all around the pivot point). However, when a system is time dependent, classical methods of finding these invariant manifolds, formally called Lagrangian Coherent Structures (LCS), do not easily apply since the flow map of the system changes over time (Haller & Yuan 2000).

One practical way of identifying LCS in time-dependent dynamical systems is by using a Finite Time Lyapunov Exponent (FTLE) field. In qualitative terms, the FTLE expresses the time average of the maximum expansion rate of a pair of particles advected in the flow (Shadden *et al.* 2005). LCS boundaries can be identified as "ridges" of high-intensity lines in the FTLE field. The method was explored by Haller (see Haller & Poje 1998; Haller & Yuan 2000) and revisited by Shadden *et al.* (2005). The main advantage of LCS analysis is that orderly structures can be revealed for a finite time interval for highly chaotic flows. These structures would not easily appear through traditional tools of analysis (Shadden *et al.* 2005).

LCS analysis has been applied to a few applications in fluid dynamics. A popular study was related to contamination accidents which can potentially affect the currents close to Monterey Bay, California (Lekien & Leonard 2004). Other applications include studies of 2D turbulent structures (Haller & Yuan 2000), hairpin vortices (Green *et al.* 2007), vortices of bio-inspired flows (Shadden *et al.* 2005), and a fully turbulent channel flow (Green *et al.* 2007). In addition Shadden *et al.* (2005) present how the the FTLE field can directly reveal the separation profile of the flow over an airfoil, while Lipinski *et al.* (2008) have presented how the FTLE field can be used to study 2D vortex-shedding over an airfoil.

The computational implementation for obtaining the LCS is based on an extensive treatise by Shadden *et al.* (2005). First, let $D \subseteq \mathbb{R}^n$ be the domain of a fluid flow with position vector $\boldsymbol{x}(t; t_0, \boldsymbol{x_0}) \in D$ and $t \in I \subset \mathbb{R}$. A dynamical system can be defined completely by the following, equations

$$\dot{\boldsymbol{x}}(t; t_0, \boldsymbol{x_0}) = \boldsymbol{v}(\boldsymbol{x}(t; t_0, \boldsymbol{x_0}), t) \tag{2.1}$$

$$\boldsymbol{x}(t_0; t_0, \boldsymbol{x_0}) = \boldsymbol{x_0} \tag{2.2}$$

The flow map $\phi_{t_0}^{t_0+t}$ can be defined as

$$\phi_{t_0}^{t_0+t}(\boldsymbol{x}) = \boldsymbol{x}(t; t_0, \boldsymbol{x_0}), \tag{2.3}$$

which describes the trajectory of a particle starting at $\boldsymbol{x_0}$ and reaching $\boldsymbol{x}$ at time $t_0 + t$. Equations 2.1 and 2.2 are solved using backward integration over a time interval T_{int}. Backward integration is used to identify attracting (unstable for time independent flows) manifolds, while forward integration can be used for repelling (i.e stable) manifolds over time (Shadden *et al.* 2005). For the flat-plate boundary layer, backward integration is used since our analysis focuses on the evolution of unstable manifold types.

In order to describe how neighbouring particles repel or attract along their trajectories, we introduce the matrix $\boldsymbol{M}(\phi_{t_0}^{t_0+t}(\boldsymbol{x_{i,j}}))$ for the neighbourhood of a particle with initial

$\mathbb{R}^2$
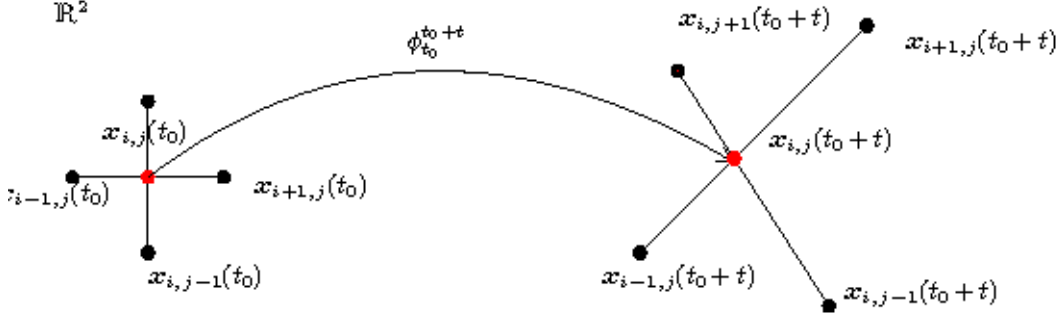

FIGURE 15. Relative stretching of neighbouring particle trajectories. Adapted from the discussion in Shadden *et al.* (2005).

position $\boldsymbol{x_0}$,

$$M(\phi_{t_0}^{t_0+t}(\boldsymbol{x}_{i,j})) = \left(\frac{d\phi_{t_0}^{t_0+t}(\boldsymbol{x})}{d\boldsymbol{x}} \right)_{\boldsymbol{x}_{ij}}. \tag{2.4}$$

The finite time version of the Cauchy deformation tensor for the same particle has the form,

$$\boldsymbol{\Delta}|_{i,j} = M^T M. \tag{2.5}$$

Maximum stretching of the neighboring particles corresponds to the maximum eigenvalue of the deformation tensor. This eigenvalue is related to the FTLE of particle $x_{i,j}$ over T_{int} according to,

$$\sigma_{t_0}^{t_0+T}(\boldsymbol{x}_{i,j}) = \frac{1}{|T_{\text{int}}|} \ln(\sqrt{\lambda_{\max}}). \tag{2.6}$$

By evaluating σ for all points $\boldsymbol{x}_{i,j}$ in the domain, an intensity FTLE field plot can be produced, and the LCS is identified as lines of high σ.

2.6. *Example of spot visualization using the Lyapunov exponent*

The time evolution of a turbulent spot, captured using the Lyapunov exponent, is shown in figures 16 and 17. The sequence spans a time interval $\Delta T = 140$ time units, based on the free-stream mean speed and the inlet boundary layer thickness. The top view (figure 16) shows a plane at distance, $y/\delta_0 = 1$ from the wall, where δ_0 is the boundary layer thickness at the inlet of the computational domain. The shown region of the flow domain captures the inception of the turbulent spot and its downstream propagation. The contours of the Lyapunov exponent clearly mark the turbulent patch. However, some of the streaky structures within the boundary layer are also visible in the figure. Edge detection schemes are still required in order to identify the edges of the turbulent spots.

In figure 16, the leading and trailing edges of the spot convect at different speeds. The former is moving downstream at a higher speed, and hence the spot grows in streamwise extent. The propagation speed of the spot 'center' is approximately $0.5 - 0.6U_\infty$, but can only be approximately inferred from the contour plot. In addition to the longitudinal spreading, the spot also spreads in the spanwise direction. A spread angle with reference to the spot trailing edge can be measured, and will be reported in subsequent sections.

Figure 17 shows the side views which correspond to the same time instants as in figure
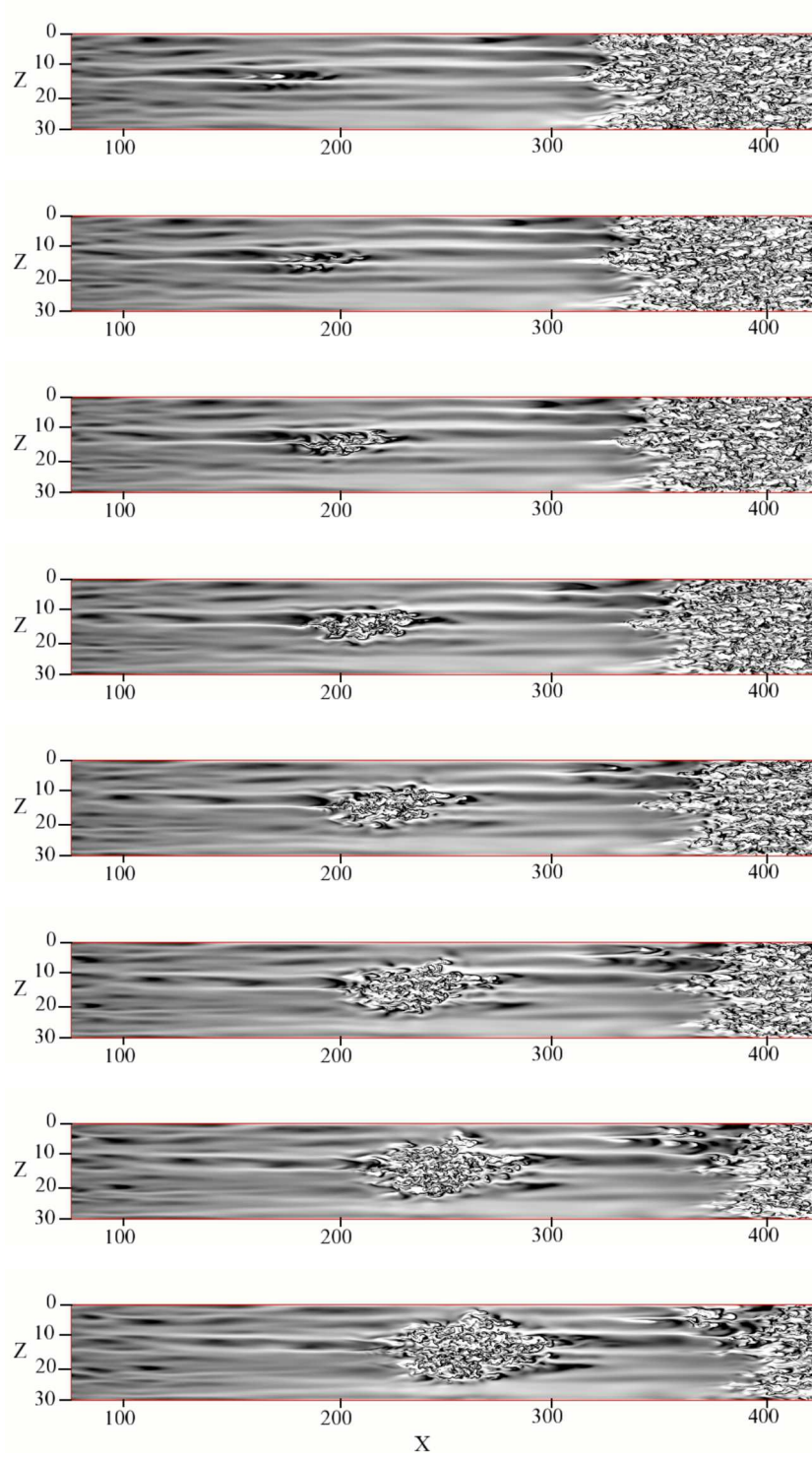
FIGURE 16. Top view of the boundary layer showing spot evolution using contours of the Finite time Lyapunov exponent.
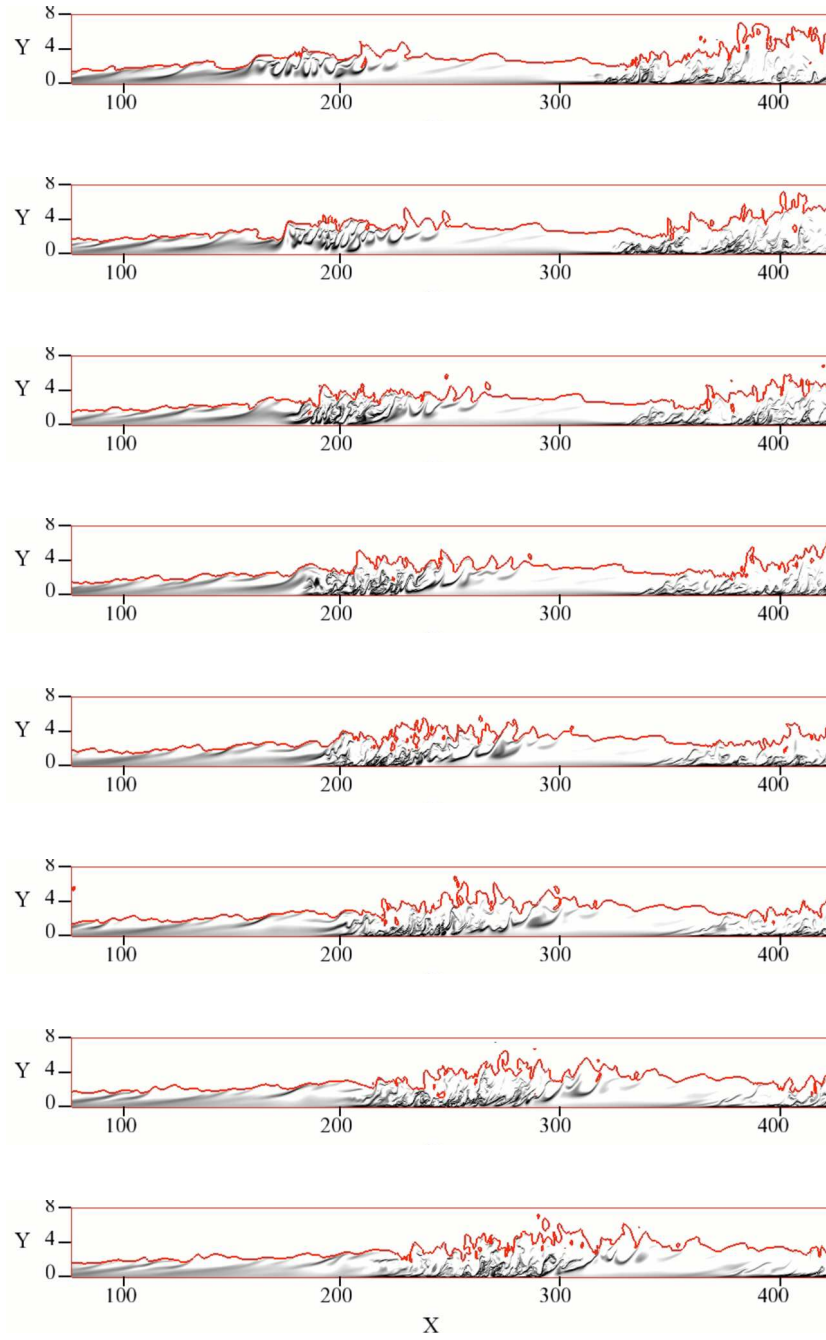
18

FIGURE 17. Side view of the boundary layer showing spot evolution using contours of the Finite time Lyapunov exponent. The snapshots are at the same time instants as in figure 16.

16. The edge of the boundary layer is marked in the figure, and is defined as the boundary layer 95% thickness. The side views clearly demonstrate that the spot is initiated near the free stream, due to an outer instability of the streaky base flow. This is the mode of breakdown reported by Jacobs & Durbin (2001). Later, Vaughan & Zaki (2010) investigated the origin of the outer instability. They carried out linear stability analyses of streaky boundary layers, when the base streaks are unsteady. They demonstrated that a spanwise sub-harmonic, parametric resonance can lead to fast growing waves. The growth rate of the instability was shown to increase with the unsteadiness of the base flow, which is the case in the current simulations because the Klebanoff distortions are generated due to free-stream vortical forcing. The time sequence in figure 17 also shows that, in the spot region, the local boundary layer thickness is increased The thickening of the boundary layer is due to the enhanced momentum mixing. As the spot convects downstream, it spreads vertically and impinges onto the wall. This impingement is followed by a strong enhancement in the turbulent intensity of the spot, and faster lateral spreading. As a result, the spread angle of the spot is expected to depend on the distance from the wall, especially in the early period of spot development.

In the computation of the Lyapunov exponent, two parameters must be prescribed, namely the integration period and time-step. Figure 18 shows an independence study of the integration time step. The total backward integration period for the computation for this spot was fixed at 80 convective time units, based on the free-stream velocity and the inlet δ_{99}. Three integration time-steps were used, $\Delta t = \{0.5, 1.0, 2.0\}$ time units. The Lyapunov exponent recomputed at the same $y-$location, and the results are in agreement.

Based on the results of the Lyapunov exponent, the propagation speed of a turbulent spot was computed since inception. Three values are reported in figure 19 versus time: the speed of the leading-edge, mid-point, and trailing-edge of the turbulent spot. The leading-edge speed is approximately 90% of the free-stream velocity. The mid-point of the spot convects downstream at 70% of the free-stream speed. Finally, the trailing edge of the spot convects at approximately 50% of the free-stream velocity. These values, computed at $y/\delta = 0.04$, are consistent with other measures in the literature based on the wall signature.

In addition, the spread angle of the turbulent spot can be computed as a function of time since inception. The results are shown in figure 20 for two planes, one near the wall, $y/\delta = 0.04$, and the second higher in the boundary layer, $y/\delta = 0.4$. The spot width is larger in the latter case. This is due to the fact that the spots originate near the free stream, and touch down onto the wall later in time. Therefore, the wall signature is initially smaller than the projection of the full spot onto the horizontal plane. Later in time, the spread angle in both the near-wall and the higher plane converge. These results stress that measurements based on the wall signal, for instance wall-stresses, do not convey the extent of the spot, particularly at the early stages of spot spreading.

The above results were based on the analysis of one particular spot. In order to obtain reliable measures of properties such as propagation speeds and spread angles, multiple spots must be processed. In the next section, a time map of the spot inception is presented. Using edge detection algorithms, spot characteristics will be obtained from the time map. In addition, the conical transformation proposed by Cantwell *et al.* (1978) will be introduced and used in the following sections in order to study the similarity between the various patches of turbulence recorded in our direct numerical simulations.
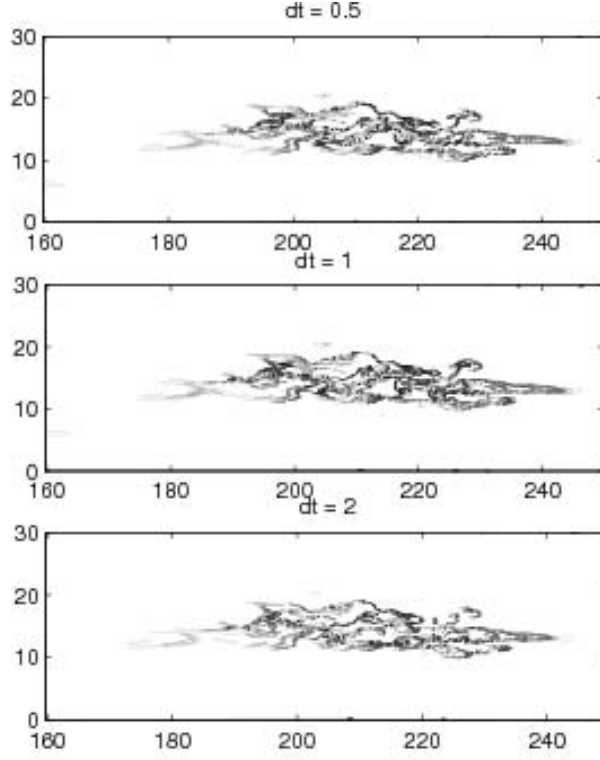
FIGURE 18. Effect of the integration time-step on the Lyapunov exponent.
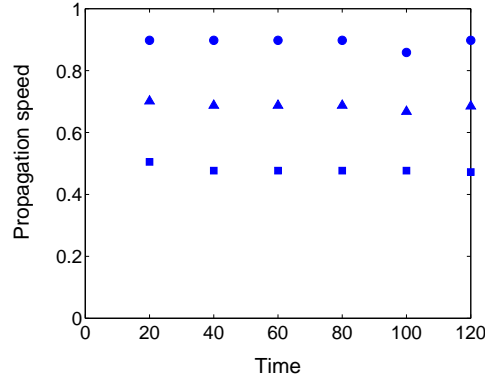
FIGURE 19. The propagation speed of a turbulent spot is plotted versus the time since inception. ○, the speed of the leading edge; △, the speed of the middle-point; □ the speed of the trailing edge.

3. Results and Discussion

3.1. *Analysis of turbulent spots from DNS database*

In order to obtain a more reliable measure for the average speeds and spread angles, a similar analysis was performed for all the spots that appear in a time period of 7,940 time units. The recorded 42 spots emerged at different locations and times. A time history
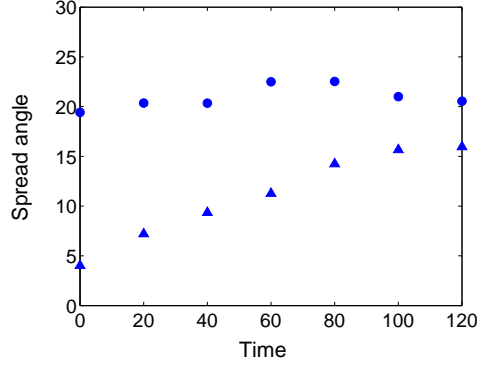
FIGURE 20. The spreading angle of a turbulent spot is plotted versus the time since inception. $\bigcirc$, the spread angle at $y/\delta = 0.4$; $\triangle$, the spread angle at $y/\delta = 0.04$.
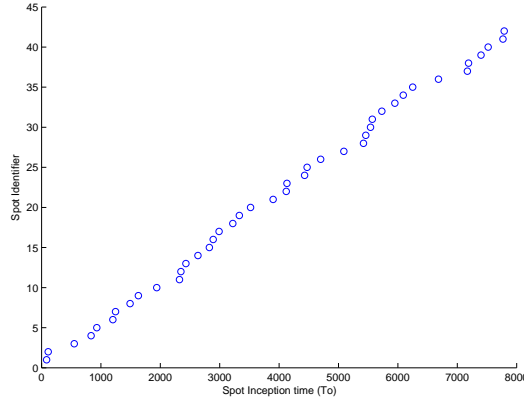
FIGURE 21. Time of spot inception versus spot identifier.

of inception is shown in figure 21. The approximately linear rate of appearance of spots corresponds to one spot per 190 time units, based on U_∞ and δ_{99}. According to the time-averaged skin friction profile (see figure 12), the length of the transition region is approximately 100 length units. Based on a propagation speed of the center of the spot of the order of $0.5U_\infty$, the lifetime of a turbulent patch is approximately 200 time units. This lifetime is consistent with the rate of inception (one spot every 190 units) shown in figure 21.

It is important to note that the spots do not develop in exactly the same pattern as the first spot shown in figures 16 and 17. Instead, they differ in terms of inception location and interference of two (or more) spots developing close to each other. A histogram and the cumulative distribution function of spot inception with respect to the different streamwise locations are given in figures 3.1a and b, respectively. Both the mean and the median are close to $x = 260$, measured relative to the inlet of the computational domain, $x_{inlet} = 33$.

The time map of the spots is shown in figure 23. It is a contour plot of the Lyapunov exponent at a particular (y, z) location, plotted as a function of (x, t). The results in figure 23 are recorded at $(y, z) = (0.1, 30)$. This line along the x-coordinate is the axis

FIGURE 22. (*a*) Histogram showing the frequency of spot inception for a range of streamwise locations; (*b*) The empirical cumulative distribution function showing the percentage of the total number of spots that were observed upstream of a given streamwise location

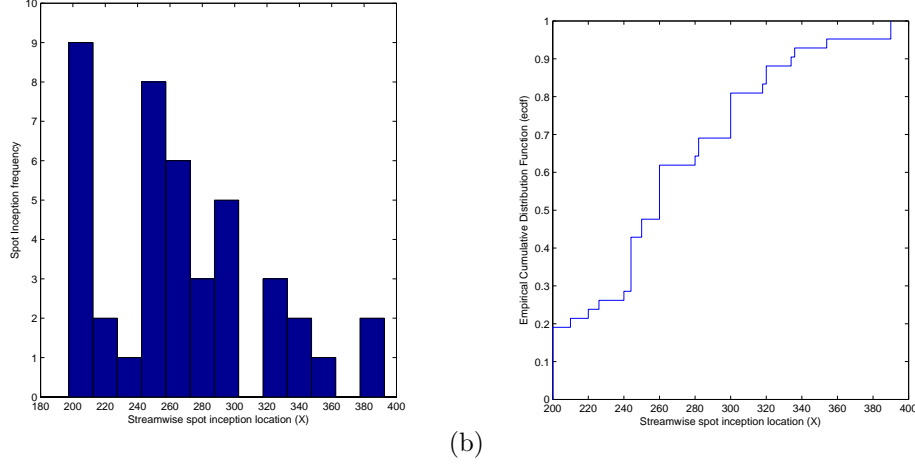of symmetry of some of the turbulent spots. Since spot inception is a function of space, similar (x, t) maps were required at the axes of symmetry of the various spots.

A zoomed-in view of figure 23 is show in figure 24(a). The latter focuses on the development of a single spot, and illustrates the linearity of growth for the trailing and leading edges of the patch of turbulence. The leading and trailing edges, denoted LE and TE respectively, are identified using edge detection techniques. The horizontal distance, $x_{LE} - x_{TE}$, is the streamwise length of the spot along its axis of symmetry. In addition, the slopes of the LE and TE lines are the propagation speeds, and are computed using linear regression. The propagation speeds for the marked spot are shown figure 24(b), where the coordinates have been shifted by t_0 and x_0, the inception time and location of the turbulent spot.

The constant speeds of propagation of the leading and trailing edges (see figure 24*b*) suggest that the spot length is linearly proportional to time. Whether all spots have a constant speed of propagation is examined using the non-dimensional variables,

$$x^* = \frac{x - x_0}{x_f - x_0} \tag{3.1}$$

$$t^* = \frac{t - t_0}{t_f - t_0} \tag{3.2}$$

where x_0 and t_0 corresponding to the virtual origin while x_f and t_f correspond to the last reliable trace for a given spot. Figure $25a - b$ show the non-dimensional coordinates for few of the turbulent spots. The results demonstrate that the leading and trailing edges indeed propagate at constant speeds independent of the choice of the spot. However, the actual speed of propagation does not need to be the same for the data to collapse on the line of unit slope.

The above methods for determining the virtual origin and the corresponding propagation speeds were applied to twelve of the 42 spots. The selected turbulent patches were most amenable to analysis using edge detection over a sufficient time period of their evolution. The remaining spots were not included in the analysis due to their merging
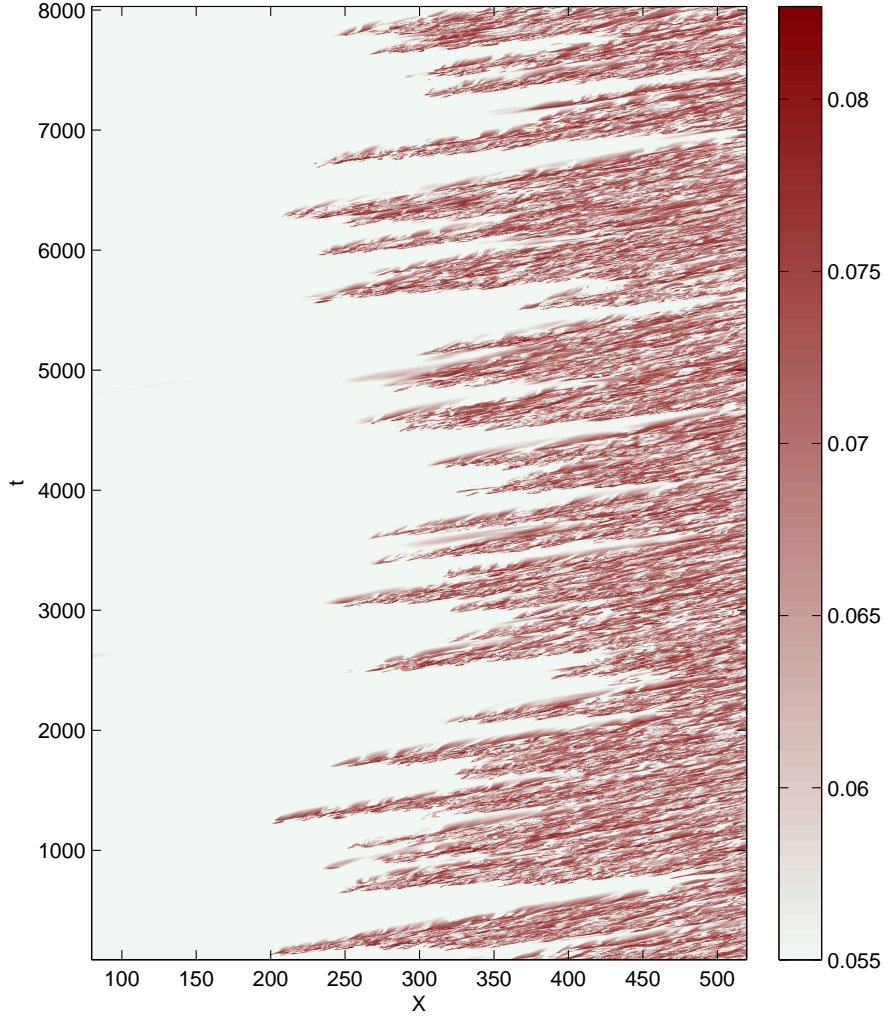
FIGURE 23. x-t time map of the FTLE domain defined by $y/\delta = 0.1$, $z = 30$ and $x/\delta \in [80, 520]$

in the streamwise or spanwise directions with adjacent patches of turbulence, or due to their late inception which resulted in early merging with the fully turbulent boundary layer downstream. The relevant results are given in table 1 and are in good agreement with the existing literature, apart from the TE speed which appears to be slightly lower than half U_∞ on average.

3.2. *The conical similarity*

Despite the random nature of the spots, previous work has sought a universal description of the evolution of these turbulent patches. In particular, Cantwell *et al.* (1978) proposed

24

(a)

(b)
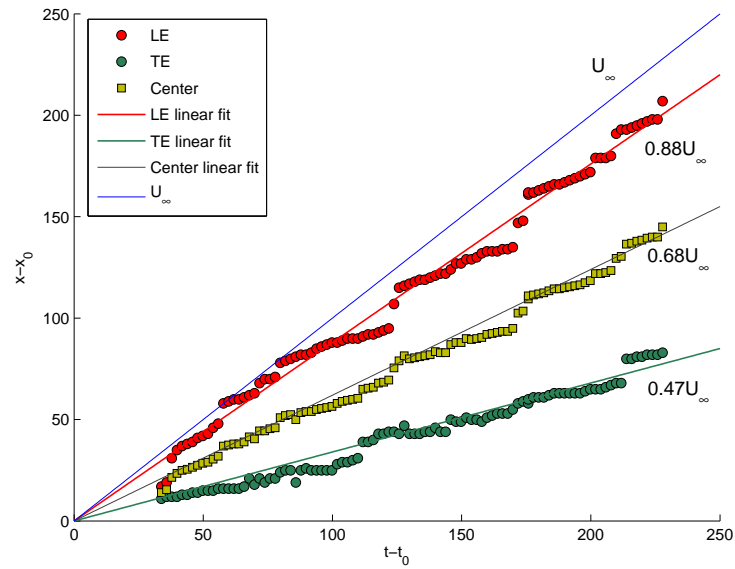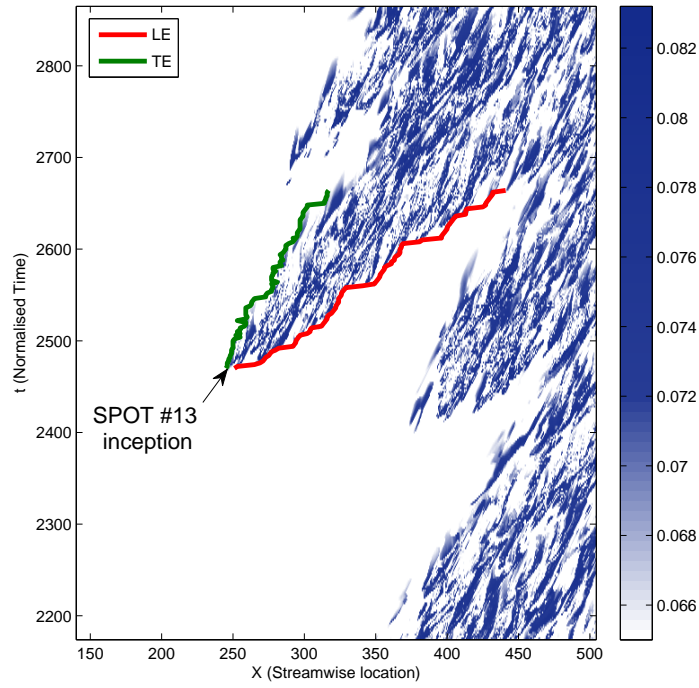
FIGURE 24. (a) Time map of a particular turbulent spot, showing the detection of the boundaries which define the leading and trailing edges. The distance $x_{LE} - x_{TE}$ corresponds to the total streamwise length of the spot along its axis of symmetry. (b) The propagation speed of the leading and trailing edge as a function of time.

(a)
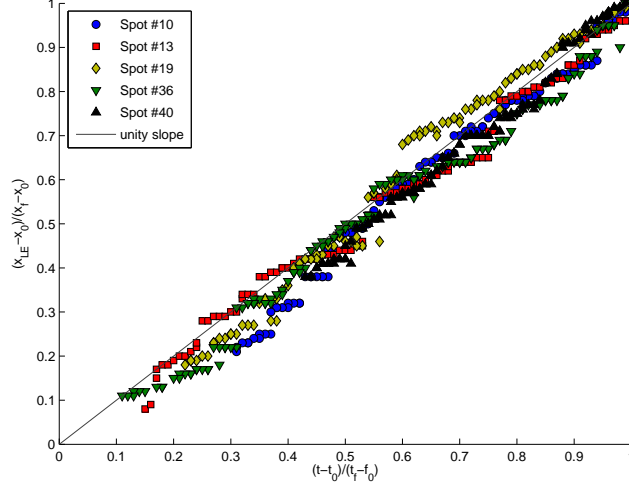
(b)
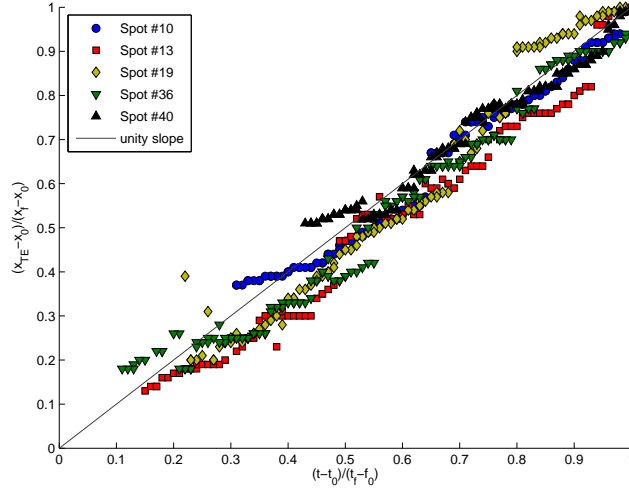
FIGURE 25. Testing the conical approximation using x^* and t^* for (a) the leading edge and (b) the trailing edge

the notion of *conical similarity*. The conical transformation rescales spots at different times during their development onto the coordinate axes defined according to,

$$\xi = \frac{x - x_0}{U_\infty(t - t_0)} \tag{3.3}$$

$$\eta = \frac{y}{U_\infty(t - t_0)} \tag{3.4}$$

$$\zeta = \frac{z - z_0}{U_\infty(t - t_0)} \tag{3.5}$$

Spot ID	Inception Time	U_{TE}/U_∞ (± 0.005)	U_C/U_∞ (± 0.005)	U_C/U_∞ (± 0.005)	α_{avrg} (± 0.05)
3	554	0.86	0.68	0.49	$19.0°$
6	1200	0.91	0.70	0.49	$18.2°$
9	1630	0.86	0.67	0.48	$21.0°$
10	1954	0.83	0.65	0.47	$23.3°$
13	2462	0.88	0.68	0.47	$19.8°$
19	3330	0.87	0.68	0.48	$20.2°$
20	3520	0.89	0.70	0.50	$21.1°$
26	4704	0.82	0.64	0.46	$23.0°$
33	5952	0.93	0.73	0.52	$19.5°$
36	6684	0.88	0.68	0.47	$20.3°$
38	7190	0.88	0.67	0.46	$20.1°$
40	7520	0.89	0.69	0.48	$18.2°$
mean		0.876	0.681	0.480	$20.31°$
std. dev.		0.030	0.020	0.020	$1.62°$

TABLE 1. Statistics of spot kinetics based on a smaple of 12 spots for $y/\delta = 0.1$

The new coordinates are the normalised propagation speeds at a specific location $(\mathbf{x}, t)$, measured relative to the reference location $(\mathbf{x}_0, t_0)$. The reference point $(\mathbf{x}_0, t_0)$ correspond to a virtual origin of an assumed linear growth. This may not coincide with the actual inception time depicted in the $x - t$ map since linear growth does not appear instantaneously at inception. In the paper of Cantwell *et al.* (1978), the transformation effectively collapsed the patches of turbulence, supporting the view of universality of spot kinematics, and self-similar evolution. Those spots, however, were generated by boundary forcing; the bottom wall of their channel was perturbed in order to induce their formation. In the current simulations, the effectiveness of the transformation in collapsing the naturally-occurring spots should be addressed.

By definition, ξ for the leading and trailing edges should be constant over time, according to the conical similarity. The value of ξ should be equal to the dimensionless propagation speed of the respective edge. Figure 26 demonstrates that the lead and trailing edge speeds of the various spots are indeed constant, and collapse using the conical transformation.

The main advantage of using the transformation is to collapse the edges of all the turbulent patches, at all instants of their lifetime, into a single self-similar shape. In figures 27 and 28, the edges of various turbulent spots are plotted in the (ξ, ζ) and (ξ, η) planes, respectively. The former is the plane view and the latter is the side view of the spots, in conical coordinates.

In the plane view, approximate agreement in the shape is observed (figure 27). The mean value of the spread angle also agrees with the statistical results based on edge detection in the (x, t) map presented earlier. However, the agreement of the spot shapes in the conical coordinates is not sufficient to assert that a universal spot shape can be identified. The same applies to the side view, in the (ξ, η) plane (figure 28). The figure captures the overhang shape better than the region of the spot near the free stream. Nevertheless, the transformation gives a reliable approximation for the basic kinematics of turbulent spots.
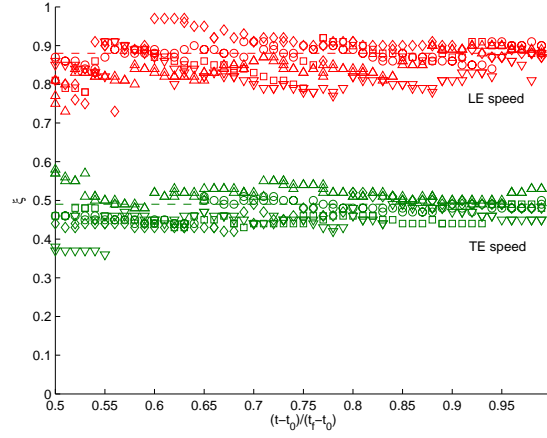
FIGURE 26. The conical coordinate ξ as the dimensionless propagation speed. Spot 10 ○; Spot 13 square; Spot 19 ◇; Spot 36 ▽; Spot 40 △
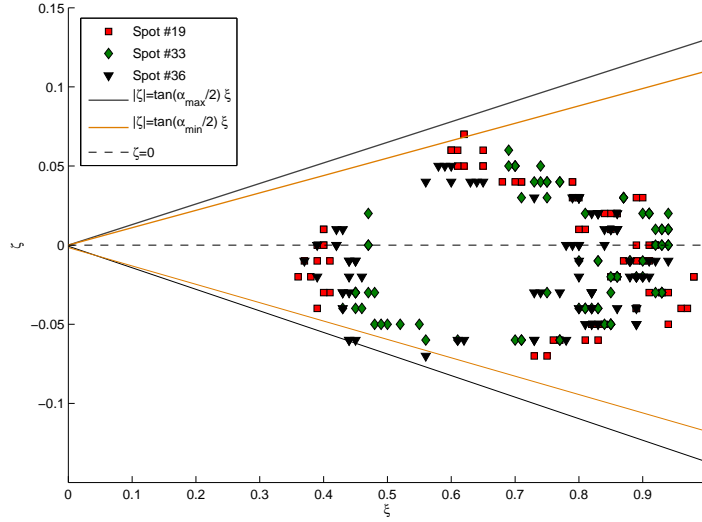
FIGURE 27. x-z edge profile of three spots transformed into conical coordinates. $\alpha_{min} = 18.69°$ and $\alpha_{max} = 21.93°$ based on the statistics of the spread angle for the al 12 Spots

3.3. *Spot structure*

The above discussion focused on the outline of the turbulent patches. Here, the vortical, turbulent structures within the spot are inspected. Often, the turbulent spot is considered to consist of an agglomeration of hairpin vortices. Vortex identification criteria were applied in order to visualize the vortex structures within the patches of turbulence. In particular, the λ_2 criterion (Jeong & Hussain 1995) was used, where λ_2 is the second

FIGURE 28. x-y edge profile of three spots transformed into conical coordinates

eigenvalue of $\mathbf{S}^2 + \mathbf{\Omega}^2$, and

$$\mathbf{S} = \frac{1}{2}[\nabla\mathbf{u} + (\nabla\mathbf{u})^T] \tag{3.6}$$

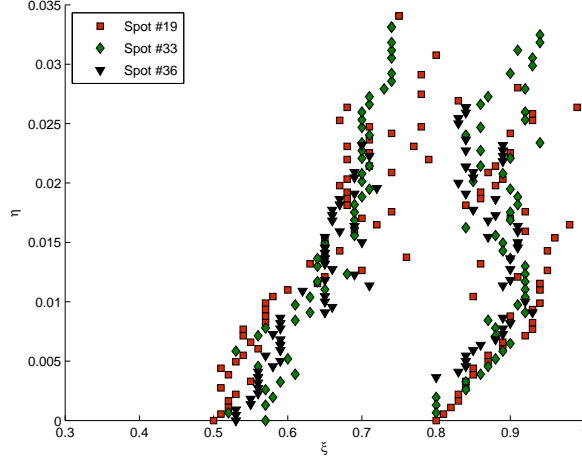$$\mathbf{\Omega} = \frac{1}{2}[\nabla\mathbf{u} - (\nabla\mathbf{u})^T]. \tag{3.7}$$

The vortical structures within the turbulent spots were visualized using iso-surfaces of the Lyapunov exponent and $\lambda_2 = -0.015$. A comparison of their top views is shown in figure 29. The general spread angle of the turbulent patch is captured by both criteria. The edges of the spot are marked by a closed line, which highlights the overlap between the two visualization techniques. This region of the spot corresponds to the main vortices which engulf, or entrain, the surrounding fluid into the turbulent spot. Away from the marked regions, and in particular in the middle of the spot, there is a lesser degree of agreement between the two criteria. This mismatch is more evident in figure 30, where a three-dimensional view of the spot is shown.

In figure 30, the agreement of the two criteria in capturing the edges of the spot is clear. In the middle, the iso-surface of λ_2 captures the presence of a row of symmetric hairpin vortices. However, the finite time Lyapunov exponent does not captures these vortical structures. The disagreement is most likely due to the choice of the backward integration time in the computation of the LCS, which was sufficiently long in order to capture the overall structure of the spot. As such, it exceeds the lifetime of the hairpin vortices which form and breakdown on a shorter time scale. Therefore, at least two backward integration times must be used in the computation of the finite-time Lyapunov exponent, in order to capture the dynamics which contribute to the evolution of the spots: The first integration time should correspond to the global evolution of the spot, and the second should address the formation and breakdown of the eddies, or vortices, within the patch of turbulence.

4. Conclusions

The interaction of free-stream turbulence with a laminar boundary layer leads to by-pass transition to turbulence. This phenomenon was simulated using direct computa-
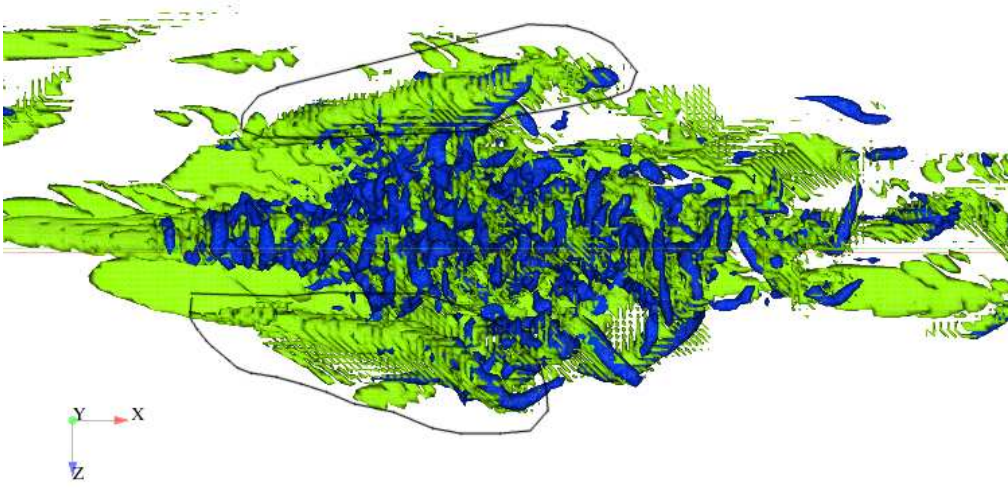
FIGURE 29. Spot 33: top view showing the iso-surface of the finite time Lyapunov exponent in green, and the iso-surface of $\lambda_2 = -0.015$ in blue. The two closed lines on the sides mark the cores of the vortical structures where the Lyapunov exponent LCS and the λ_2 isosurface overlap.
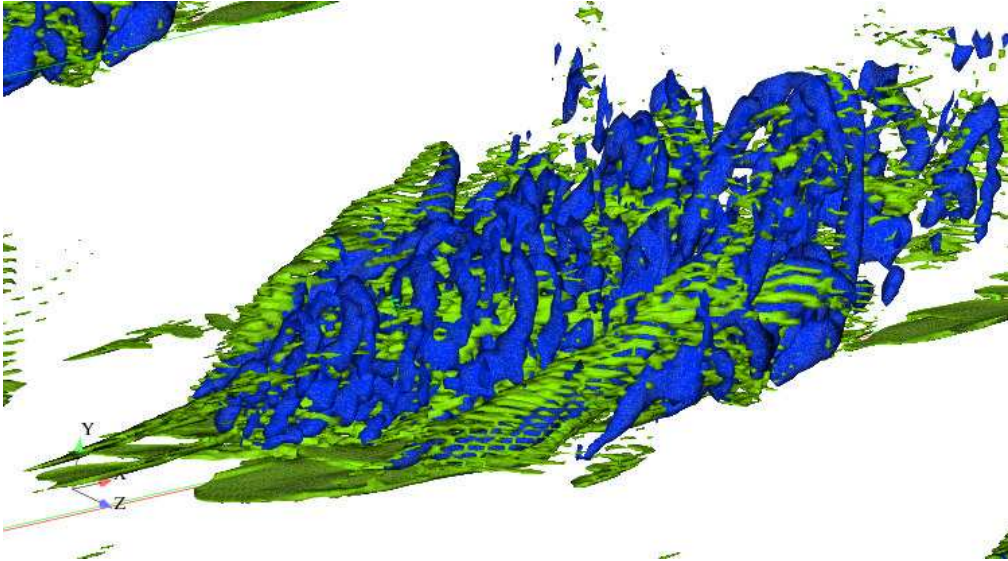
FIGURE 30. Spot 33: three-dimensional view showing the iso-surface of the finite time Lyapunov exponent in green, and iso-surface of $\lambda_2 = -0.015$ in blue.

tions of the Navier-Stokes equations. The numerical simulations capture the proceedings of transition: Klebanoff streaks amplify within the boundary-layer shear, followed by their secondary instability and finally the formation of turbulent spots which spread and merge downstream. A time sequence spanning $7,940$ time units was stored during the simulations. This period captured the evolution of 42 turbulent spots. Twelve of these turbulent patches were clearly identifiable, without interaction with neighboring spots.

In order to study the evolution of the turbulent spots, various visualization techniques were considered, for example based on the three components of perturbation velocity and vorticity. The streamwise velocity, and also the wall-normal vorticity are not well suited for inspection of the spot shape due to the high-amplitude streaks. Instead, the other components of the perturbation field can be used. One major drawback of this approach, however, is the subjective definition of the spot. In the literature, a level of perturbation velocity is often used to define the spot, for instance $\|v'\| > 3\%$. It was demonstrated that the spot spread angle is sensitive to this definition by comparing three values of the threshold. This measure must also be adjusted in the vicinity of the wall since the perturbation velocities decays in the near-wall region. The use of the finite time Lyapunov exponent in order to determine the structure of the turbulent spots was investigated. It was demonstrated that the method can capture the turbulent patches, without any clutter due to the Klebanoff streaks.

An $x - t$ map of the turbulent patches was computed, using contours of the finite-time Lyapunov exponent. Edge detection techniques of the map yielded the propagation speeds of the leading and trailing edges, which agreed with the literature. In addition, the conical transformation was verified for the naturally-triggered spot. It was shown that the shape of the various patches of turbulence can collapse into a self-similar shape.

Finally, a comparison of the λ_2 vortex identification criterion and the finite-time Lyapunov exponent was presented. Agreement in the prediction of both techniques was only observed near the edges of the spots. These edge-vortices play a significant role in the global dynamics of spot spreading. However, the internal structure of the spot, namely the hairpin vortices, were only captured by the λ_2 criterion. This was attributed to the relatively short time scale of the formation and breakdown of the hairpin vortices, in comparison to the backward integration time used in the computation of the FTLE.

REFERENCES

ANDERSSON, P., BRANDT, L., BOTTARO, A. & HENNINGSON, D. S. 2001 On the breakdown of boundary layers streaks. *Journal of Fluid Mechanics* **428**, 29–60.

CANTWELL, B., COLES, D. & DIMOTAKIS, P. 1978 Structure and entrainment in the plane of symmetry of a turbulent spot. *Journal of Fluid Mechanics Digital Archive* **87** (04), 641–672.

GREEN, M. A., ROWLEY, C. W. & HALLER, G. 2007 Detection of lagrangian coherent structures in three-dimensional turbulence. *Journal of Fluid Mechanics* **572** (1), 111–120.

GAD-EL HAK, M., BLACKWELDER, R. F. & RILEY, J. J. 1981 On the growth of turbulent regions in laminar boundary layers. *Journal of Fluid Mechanics* **110**, 73–95.

HALLER, G. & POJE, A. C. 1998 Finite time transport in aperiodic flows,. *Physica D: Nonlinear Phenomena* **119** (3-4), 352–380.

HALLER, G. & YUAN, G. 2000 Lagrangian coherent structures and mixing in two-dimensional turbulence. *Phys. D* **147** (3-4), 352–370.

JACOBS, R. G. & DURBIN, P. A. 2001 Simulations of bypass transition. *J. Fluid Mech.* **428** (01), 185–212.

JEONG, J. & HUSSAIN, F. 1995 On the identification of a vortex. *Journal of Fluid Mechanics* **285**, 69 – 94.

Johnson, M. 2001 On the flow structure within a turbulent spot. *International Journal of Heat and Fluid Flow* **22** (4), 409 – 416, shear rates;.

Jones, L. E., Sandberg, R. D. & Sandham, N. D. 2008 Direct numerical simulations of forced and unforced separation bubbles on an airfoil at incidence. *Journal of Fluid Mechanics* **602**, 175–207.

Krishnan, L. & Sandham, N. 2006 On the merging of turbulent spots in a supersonic boundary-layer flow. *International Journal of Heat and Fluid Flow* **27** (4), 542 – 550, special Issue of The Fourth International Symposium on Turbulence and Shear Flow Phenomena - 2005.

Krishnan, L. & Sandham, N. D. 2007 Strong interaction of a turbulent spot with a shock-induced separation bubble. *Physics of Fluids* **19** (1), 016102.

Lekien, F. & Leonard, N. 2004 Dynamically consistent lagrangian coherent structures. In *American Inst. of Physics: $8^t h$ Experimental Chaos Conference* (ed. S. Boccaletti, O. Yordanov, R. Meucci, L. M. Pecora, J. Kurths & B. J. Gluckman), , vol. 742, pp. 132–139. AIP.

Lipinski, D., Cardwell, B. & Mohseni, K. 2008 A lagrangian analysis of a two-dimensional airfoil with vortex shedding. *Journal of Physics A: Mathematical and Theoretical* **41** (34), 344011 (22pp).

McAuliffe, B. R. & Yaras, M. I. 2008 Numerical study of turbulent-spot development in a separated shear layer. *Journal of Turbomachinery* **130** (4), 041018.

Riley, J. & Gad-el Hak, M. 1985 The dynamics of turbulent spots. *Frontiers in Fluid Mechanics* pp. 123–155.

Sabatino, D. & Smith, C. 2008 Turbulent spot flow topology and mechanisms for surface heat transfer. *Journal of Fluid Mechanics* **612** (-1), 81–105.

Shadden, S. C., Lekien, F. & Marsden, J. E. 2005 Definition and properties of lagrangian coherent structures from finite-time lyapunov exponents in two-dimensional aperiodic flows. *Physica D: Nonlinear Phenomena* **212** (3-4), 271–304.

Swearingen, J. D. & Blackwelder, R. F. 1987 The growth and breakdown of streamwise vortices in the presence of a wall. *J. Fluid Mech.* **182**, 255–290.

Vasudevan, K., Dey, J. & Prabhu, A. 2001 Spot propagation characteristics in laterally strained boundary layers. *Experiments in Fluids* **30**, 488–491.

Vaughan, N. J. & Zaki, T. A. 2010 Stability of zero-pressure-gradient boundary layer distorted by Klebanoff streaks. *Submitted* .

Wygnanski, I., Sokolov, M. & Friedman, D. 1976 On a turbulent in a laminar boundary layer. *Journal of Fluid Mechanics Digital Archive* **78** (04), 785–819.

Zaki, T. A., Durbin, P. A., Wissink, J. & Rodi, W. 2009 Direct computations of boundary layers distorted by migrating wakes in a linear compressor cascade. *Flow, Turbulence and Combustion* **83** (3), 307–322.

Zaki, T. A., Wissink, J., Rodi, W. & Durbin, P. A. 2010 Direct numerical simulation of transition in a compressor cascade: The influence of free-stream turbulence. *Journal of Fluid Mechanics* p. In Press.